Statistical analysis of dislocation substructure in commercially pure aluminum subjected to static and dynamic high pressure torsion

Lanjewar, Harishchandra; Naghdy, Soroosh; Verleysen, Patricia; Kestens, Leo A.I.

Important note
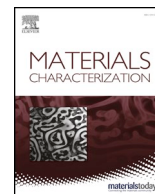To cite this publication, please use the final published version (if applicable).
Please check the document version above.

Statistical analysis of dislocation substructure in commercially pure aluminum subjected to static and dynamic high pressure torsion

Harishchandra Lanjewar[a,*], Soroosh Naghdy[a], Patricia Verleysen[a], Leo A.I. Kestens[a,b]

[a] Research Group Materials Science and Technology, Department of Electromechanical, Systems and Metal Engineering, Ghent University, Belgium
[b] Department of Materials Science and Engineering, Delft University of Technology, the Netherlands

ABSTRACT

Severe plastic deformation imposed under high hydrostatic pressure introduces a considerable dislocation substructure in metals from the early stages of deformation, ultimately resulting in grain fragmentation. Characterization and quantification of the substructure require methods with a sufficiently high angular and spatial resolution to reveal the local heterogeneities in orientation differences and the length scales of the substructure. However, the statistical relevance of the observations should be assured which requires relatively large fields of view. In present work, the evolution of dislocation substructures during static and dynamic high pressure torsion processing of commercially pure aluminum is examined. Orientation data obtained by electron backscatter diffraction using two different mapping step sizes are utilized to assess the detection of the dislocation substructures and boundaries during the grain fragmentation stage.

Accumulation of distortion in the crystal produces an increase in measurement noise at each pixel which is estimated using Kamaya's plots. The storage of dislocations and related angular misfits reduces the peak height of the probability density distribution of misorientation gradients, moves the peak to higher misorientation gradients and widens the distribution. Superposition of double Rayleigh distributions over the combined dislocation boundary data predicts a slightly higher median for the frequency of geometrically necessary boundaries and larger misorientation gradients across these boundaries in dynamically deformed material. In incidental dislocation boundaries, higher misorientation gradients are only observed at lower equivalent strains. Buildup of shear strain leads to the deterioration in the quality of the fitting to a double Rayleigh distribution and is linked to the complex evolution pattern of the dislocation boundaries. Finally, in statically deformed material, anisotropy in the substructure evolution is observed in the shear and radial planes.

1. Introduction

High pressure torsion (HPT) is one of the most commonly used methods of severe plastic deformation (SPD) which is mainly due to its unique ability to impart extremely large strains in one single operation. Indeed, in most other SPD processes such as equal channel angular extrusion (ECAE) introduced by Segal [1,2] and accumulative roll bonding (ARB) proposed by Saito et al. [3], the deformation is imposed in discrete steps. Though already proposed by Bridgman in the early 1950s [4], HPT was reintroduced in the 90s [5] as a SPD process that imposes continuous torsion deformation on a disk sample under high axial pressure. As a result, a very fine grain structure is obtained in metals with a multitude of enhanced and interesting properties, especially strength and superplastic forming [6]. Additionally, the grain boundary (GB) area in SPD materials, though less than 1%, has a non-

equilibrium structure and affects the material properties owing to its modified kinetic and thermodynamic characteristics [7].

SPD performed at either high strain rate or low temperature is known to produce enhanced dislocation density, thereby generating much finer cell structure [8]. In addition to inhibiting thermally stimulated relaxation processes, high strain rate deformation may raise local flow stresses to very high values, triggering deformation twinning even in materials with high stacking fault energy. Thus, multiple deformation mechanisms acting to accommodate the deformation, lower the strain levels needed to achieve the same refined microstructure as that obtained in low strain rate SPD methods. Recently, a dynamic HPT (DHPT) method capable of imposing torsional strain rates of the order of 10,000 s^{-1} was introduced and found to refine the original coarse grains of commercially pure aluminum slightly faster than conventional HPT [9]. Present work primarily deals with the evaluation of the

dislocation substructures and boundaries formed in the fragmenting grains as a result of deformations imposed during HPT and DHPT methods.

For most metals, the process of grain fragmentation is governed by dislocations or more specifically the interaction between dislocations. In order to describe and characterize the dislocation structures which form as a result of moderate strains, a general framework was provided by Kuhlmann-Wilsdorf [10]. This was further extended by Hansen to the large strains normally observed in cold rolling and drawing operations [11]. In deformation structures, the most easily distinguishable feature is the "mosaic block" structure, which is formed when two almost dislocation free regions are separated by dislocation cell boundaries (CBs). These cells together form individual domains bounded by extended cell block boundaries (CBBs). The cell boundaries are the aggregates of incidental or statistically stored dislocations (SSDs) and therefore, denoted as incidental dislocation boundaries (IDBs). The cell block boundaries, on the other hand, are composed of geometrically necessary dislocations (GND) and called as geometrically necessary boundaries (GNBs). This means that the misorientation across IDBs is due to the rigid rotations of the two neighboring volume elements. In the case of GNBs, on the contrary, different active slip systems, changes in shear amplitudes or local strain differences between two neighboring regions produce the necessary misorientation [12]. With increasing strain, the spacing between the GNBs decreases, bringing down the number of dislocation cells contained within and their size. Simultaneously the misorientations across both IDBs and GNBs increase, causing widening of the misorientation angle distribution [11]. Generally, IDBs are characterized by a lower misorientation angle, narrow distribution of the angles and a random distribution of the misorientation axes. In contrast, the GNBs display larger average misorientations, a wider distribution of the angles and misorientation axes clustered around preferred axes [13]. Hughes et al. observed a strain-independent scaling behavior for the misorientation angle (θ), in case of both IDBs and GNBs, when θ is normalized using the mean misorientation angle, $\bar{\theta}$ as a scaling parameter, resulting in the following equation [14]:

$$P(\theta, \quad \bar{\theta}) = \bar{\theta}^\eta f\left(\frac{\theta}{\bar{\theta}^\delta}\right) \tag{1}$$

where P is the probability density distribution for misorientation angles. δ and η are exponents of the scaling parameter having values of 1 and -1, respectively. A similar scaling behavior was observed for the relative probability of the measured link lengths, i.e. dislocation line lengths between two nodes when scaled with respect to the average link lengths [15]. Thus the entire process of the formation of dislocation rotation boundaries can be characterized by the mean misorientation angle ($\bar{\theta}$). Pantleon and Hansen [13] later observed that the probability density distributions of the misorientation angles developed across IDBs and GNBs can be easily described by a Rayleigh distribution:

$$f_R(\theta) = \frac{\theta}{\sigma^2} \exp\left(-\frac{\theta^2}{2\sigma^2}\right) \tag{2}$$

where $\sigma = \sqrt{\frac{2}{\pi}}\bar{\theta}$ is the standard deviation of the distribution. The experimental data for their study were collected separately for IDBs and GNBs using transmission electron microscopy (TEM), which only allows obtaining local data from images with limited field size. Other microstructural observation techniques such as electron backscatter diffraction (EBSD) do not allow to distinguish between the boundary type, i.e. IDB or GNB, however, much larger sample areas are scanned. In case that all the boundaries are characterized together, structural parameters on separate boundaries can still be obtained by considering a Rayleigh distribution for each boundary type. The probability density distribution of all the misorientation angles is then fitted by superposing two Rayleigh distributions adopting the following equation:

$$f_{sum}(\theta) = \xi_{GNB}\left[\frac{\theta_{GNB}}{\sigma_{GNB}^2}\exp\left(-\frac{\theta_{GNB}^2}{2\sigma_{GNB}^2}\right)\right] + \xi_{IDB}\left[\frac{\theta_{IDB}}{\sigma_{IDB}^2}\exp\left(-\frac{\theta_{IDB}^2}{2\sigma_{IDB}^2}\right)\right] \tag{3}$$

where ξ_{GNB} and ξ_{IDB} ($\xi_{IDB} = 1 - \xi_{GNB}$) are the relative fractions, θ_{GNB} and θ_{IDB} the misorientation angles, and σ_{GNB} and σ_{IDB} the standard deviations of the GNBs and IDBs, respectively. Thus fitting of the double Rayleigh distribution provides the fraction and mean misorientation for either kind of boundaries. Recently, Moussa et al. proposed to use the orientation imaging maps obtained from conventional EBSD measurements and to fit the double Rayleigh distribution over the misorientation gradients ($d\theta/dx$) calculated using kernel average misorientation (KAM) data [16,17]. This uncovered a new approach where sufficiently large EBSD maps obtained at suitable step sizes could provide statistically relevant values of relative frequencies of dislocation rotation boundaries and the associated mean misorientation gradients.

The misorientation angles developing across low energy dislocation structures (LEDS), subsequent to the mutual interaction of dislocations, are treated as a result of fluctuations in the number of mobile dislocations [15,18]. Thus determination of the dislocation densities formed within the original coarse grains is crucial for the evaluation of evolutionary stages of deformation and their relation with the recrystallization mechanisms during SPD [19]. Nye proposed that the local dislocation density tensor (α) is determined entirely by the elastic distortion tensor and is related with the dislocations emanating from operative slip systems as given by [20]:

$$\alpha = \sum_{t=1}^{N} \rho^t(b^t \otimes v^t) = -curl\,\beta^e \tag{4}$$

where ρ is the dislocation density, $\boldsymbol{b}$ the Burgers vector, $\boldsymbol{v}$ the dislocation line vector for each slip system t, N is the total number of slip systems and $\beta^e = \varepsilon^e + \omega^e$ is the sum of the elastic strain tensor and the lattice rotation tensor [21]. However, Eq. (4) remains under-constrained and may possess multiple possible solutions, leading to the requirement of optimization in order to obtain the nearest possible solution for the geometrically necessary dislocation density (GNDD). Kubin and Mortensen, based on a strain gradient model, proposed a quite simple relation to relate the lattice curvature observed during plastic deformation with GNDD [22]:

$$\rho_{GND} = \frac{\chi\theta}{bx} \tag{5}$$

where χ is a constant which depends on the dislocation character and x is the distance over which the misorientation θ between the neighboring points is calculated.

However, the dislocation densities obtained by Eq. (5) are inherently sensitive to the measurement noise. The uncertainty in orientation measurement in undeformed material is known to be sensitive to the crystal orientation. On the introduction of strain, measurement noise worsens owing to the presence of dislocation content in the structure. This is because the distortion of crystal lowers the quality of Kikuchi diffraction patterns, making the detection of these bands and subsequent indexing less accurate [23]. Another problem is the pattern overlap in heavily deformed samples, whereby a large fraction of boundaries with low misorientation angles and very narrow spacing are present. All these complexities may result in a strong increase of the fraction of non-indexed points in EBSD measurement with accumulating strain in the material [23].

Further, the GNDD in the material as a function of imposed deformation strain is dependent on the Burgers circuit size, corresponding to the step size or kernel size in EBSD assessment, which separates the GNDs from SSDs [24]. Though the presence of an individual dislocation may introduce a deformation field in the material, at larger length scale any geometric perturbations caused by the SSDs is negated by the dislocations of the opposite sign within the Burgers circuit. Hence a change in the number of dislocations which are geometrically necessary
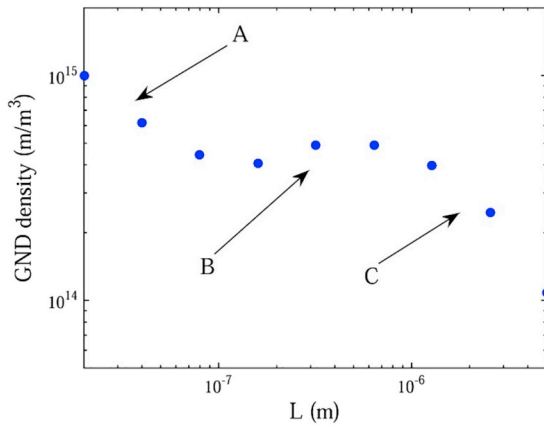
Fig. 1. The average GNDD calculated at different step sizes for an area near the indenter tip for micro-indented single crystal tantalum. Three discrete regions – (A), (B) and (C) are indicated [25].

depends on the size of the Burgers circuit that is considered [19]. As a result, as shown in Fig. 1 from ref. [25], a different GNDD is obtained with a change in EBSD step size (L). In the figure three distinct regions (A), (B) and (C) are labeled. Region (A) at small and (C) at large step size corresponds to a $1/L$ relationship [26]. Such a relationship in region (A) produces dislocation densities dominated by noise [24]. Only at the moderate step sizes in region (B), the constant GNDD represents the true GNDs accommodating the local strain heterogeneities at the same length scale as the substructure [25,27]. For the single crystal tantalum as shown in Fig. 1, region (B), corresponding to the true GND, extended from ~0.1 to 1 μm, while for commercial purity aluminum deformed using HPT at equivalent strains (ε_{eq}) from 1 to 50, the plateau was observed between 80 and 320 nm [19]. The appearance of these regions and their transition is dependent on the nature and the level of deformation of the sample [28]. Hence in order to arrive at region (B) for the HPT and DHPT deformed samples in present work and assist in the ensuing structural parameter analysis of the dislocation boundaries, EBSD assessment is performed at two mapping step sizes with a difference of an order of magnitude.

In HPT material, though shear plane surface is characterized mostly to follow the progression of microstructure, anisotropy in grain morphology exists between the shear and radial planes [29]. The microstructure evolution during HPT is known to evoke an anisotropic mechanical response in the material. In a recent study, a single-phase Ti45Nb alloy in HPT deformed condition, when tested in a tensile test exhibited anisotropic mechanical behavior in the samples extracted along the shear and axial directions [30]. Higher yield and tensile strength were observed in the shear direction, while the results for orientation dependence of material ductility were inconclusive. However, in commercially pure aluminum, anisotropy in true fracture strain values corresponding to the radial and axial directions was observed in a sample extracted along the shear direction [31]. In this case, such behavior was attributed to the lingering presence of prior rolling and recrystallization texture at lower HPT strain and at a later stage to the evolution of different shear texture components.

The main aim of present work is to perform a detailed microstructural investigation to differentiate between the evolutions of the dislocation substructure in statically and dynamically deformed commercial purity aluminum during high pressure torsion. Additionally, an effort is made to address the open question on the suitable step size for the statistical dislocation and dislocation boundary analysis from EBSD maps of metals on which large plastic strains are imposed to refine the microstructure. To that purpose, the orientation imaging data was utilized to generate the misorientation gradient maps. Statistical analysis of the probability density distributions of the misorientation gradient using a double Rayleigh distribution allowed to determine the

relative frequencies of the GNBs and IDBs, and their respective misorientation gradients. Next, the GNDD responsible for the generation of independently deforming crystal domains bounded within the high angle grain boundaries was determined. The misfit angles of the boundaries gave an idea about the stored energies in the statically and dynamically deformed materials. Finally, the substructure evolution on the shear and radial planes was investigated in a HPT deformed sample at different radial locations. Special attention was paid to detect anisotropy in the microstructural changes taking place on these planes with the progression of imposed deformation.

2. Material and methods

Commercially pure aluminum was used as the study material and was obtained in the form of cast blocks. The chemical composition was determined using atomic absorption spectroscopy (AAS) and the material contained about 99.62% of Al while remaining impurities included 0.28% Fe, 0.05% Si and 0.05% Cu. The cast blocks were cold rolled to a thickness of 1.3 mm and then annealed at 773 K for 30 s, producing an average recrystallized and strain-free grain size of 85 μm. Disk samples of 15 mm diameter and ring samples having an outer diameter of 11 mm and ring width of 3 mm were used for HPT and DHPT experiments, respectively.

The schematics of the experimental setup used in the present investigation are as shown in Fig. 2. The HPT deformation is imposed in semi-constrained condition under an axial pressure of 2.5 GPa and rotational speed of 1 rpm. The sample reference system in simple shear deformation mode as indicated in Fig. 2 (c) consists of three directions namely, radial (*RD*), shear (ϕ) and shear plane normal (*Z*). The equivalent strain introduced in the material is given by:

$$\varepsilon_{eq} = \frac{2\pi N r}{\sqrt{3}\, h} \tag{6}$$

where N is the number of revolutions applied to the sample, r is the radial distance from the center axis and h is the thickness of the sample.

Like HPT, the deformation in DHPT is applied under semi-constrained conditions and the applied strain is assessed using Eq. (6). The ring sample is held under an axial pressure of 1.4 GPa, in an annular groove machined into the mold having a depth of 0.3 mm on each surface. As shown in Fig. 2 (b), almost the entire length of the incident bar is pre-torqued in order to increase the amount of elastic energy stored in the bar and the torsional pulse width. The friction clamp system held together by a notched high strength steel bolt is placed near the sample containing molds. The pneumatic system provided at the friction clamp mechanism is used to break the bolt, releasing the stored torsional energy and thus applying high-speed torsional deformation to the sample material. The rotational speed acting on the mold at the incident bar is given by:

$$\dot{R}_{in} = \frac{T_i - T_r}{Z_{b,in}} \tag{7}$$

where T_i is the incident torque amplitude, T_r the reflected torque amplitude, and $Z_{b,\,in} = \rho_b C_b J_b$, the torsional impedance of the input bar, ρ_b the density of bar material, C_b the speed of wave propagation in torsion, and J_b the polar moment of inertia for a cylindrical bar. From the condition of torque equilibrium within the sample, the strain rate applicable at different radial locations r can be assessed by the following relation [9]:

$$\dot{\varepsilon}_{vM} = \frac{1}{\sqrt{3}} \frac{2T_i - T_{sample}}{Z_{b,in}} \frac{r}{h} \tag{8}$$

where T_{sample} is the torque required to deform the sample material. In DHPT, the strain rates when calculated using a mean radius of 4 mm, were of the order of 10^3 s^{-1}. The combined effect of the deformation temperature and strain rate is most often represented by the Zener-
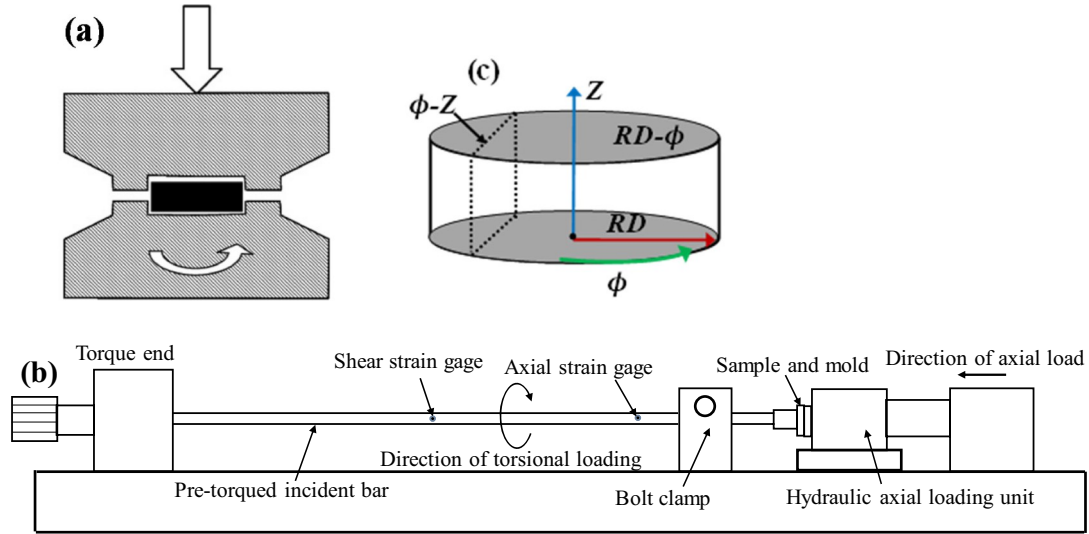
Fig. 2. Schematics of the experimental setups used in the present study - (a) semi-constrained high pressure torsion [6], and (b) dynamic high pressure torsion (DHPT) [9,32] and (c) sample reference frame with cylindrical coordinate axes: radial (*RD*), shear (ϕ) and shear plane normal (*Z*). The planes of microstructural observation, shear plane (*RD-ϕ*) and radial plane (ϕ-*Z*) are distinguished by their normal directions – *Z* and *RD*, respectively.

Hollomon parameter, $Z = \dot{\varepsilon}\, e^{\left(\frac{Q}{RT}\right)}$, where Q is the activation energy and R the gas constant [33]. The applied deformation conditions in DHPT at the room temperature resulted in a Zener-Hollomon parameter (ln Z) of ~70, using a value 156 kJ/mol for Q from ref. [34].

The microhardness measurements were performed on the HPT and DHPT samples on the *RD-ϕ* plane using a Vickers diamond indenter with a load of 300 gf and a dwelling period of 15 s, on a LECO AMH43 hardness testing machine. The hardness values were measured as an average of three indents, lying at a distance of ~0.2 mm at each radial location.

The orientation imaging microscopy (OIM) measurements were carried out on the ϕ-*Z* plane using an EBSD system mounted on a scanning electron microscope with a field emission gun of type FEI-Quantax®. The sample preparation included fine mechanical polishing followed by electropolishing using Struers A2 electrolyte at a voltage of 45 V for 10 s. The EBSD maps were collected at a tilt angle of 70°, the working distance of 16 mm, accelerating voltage of 15 kV and step sizes of 0.1 and 1 μm. The microstructural investigations were performed using mapping areas of 100×100 and 500×500 μm^2 for 0.1 and 1 μm step sizes, respectively. TSL OIM™ software was used for the post-processing of the data and microstructural analysis. The post-processing data clean up included removal of pixels with confidence index lower than 0.1 followed by grain confidence index standardization and a single iteration of grain dilation.

3. Experimental results and discussion

3.1. Effect of EBSD mapping step size

The experimentally observed probability density (*P*) and accumulated frequency (*f*) distributions are displayed in Fig. 3, for EBSD mapping data acquired at two different step sizes, i.e. 0.1 and 1 μm for the DHPT samples, in order to differentiate between the substructures resolved. The kernel average misorientation data was collected for 1 to 5 neighbors. As can be seen from *P* distributions for both 0.1 and 1 μm, in Fig. 3 (a) and (b) respectively, with increasing ε_{eq} the distribution peak P_{max} lowers and moves to higher misorientation gradients with widening observed in the distribution. Such behavior is quite similar to that observed for misorientations for both IDBs and GNBs when characterized individually using TEM [14]. This, however, occurs with significant differences between the misorientation gradients developed

at these two step sizes. These experimental distributions when fitted by superposing two Rayleigh distributions using the following equation for probability density distribution:

$$f_{sum}(\theta) = \xi_{GNB}\left[\frac{(d\theta/dx)_{GNB}}{\sigma_{GNB}^2}\exp\left(-\frac{(d\theta/dx)_{GNB}^2}{2\sigma_{GNB}^2}\right)\right] + \xi_{IDB}\left[\frac{(d\theta/dx)_{IDB}}{\sigma_{IDB}^2}\exp\left(-\frac{(d\theta/dx)_{IDB}^2}{2\sigma_{IDB}^2}\right)\right]$$

(9)

or for accumulated frequency distribution:

$$f_{accumulated}(\theta) = \xi_{GNB}\left[1 - \exp\left(-\frac{(d\theta/dx)_{GNB}^2}{2\sigma_{GNB}^2}\right)\right] + \xi_{IDB}\left[1 - \exp\left(-\frac{(d\theta/dx)_{IDB}^2}{2\sigma_{IDB}^2}\right)\right]$$

(10)

it is possible to determine the standard deviation (σ) of individual distributions of GNB and IDB and fraction of each of these boundaries, ξ_{GNB} and ξ_{IDB}. Knowledge of σ in a Rayleigh distribution allows calculation of mean misorientation gradient using relation:

$$\overline{\frac{\Delta\theta}{\Delta x}} = \sigma\sqrt{\frac{\pi}{2}}$$

(11)

The modeled structural parameters of the dislocation structure are given in Table 1 and the mean misorientation gradients, for IDBs and GNBs at both the step sizes, are plotted vs. ε_{eq} in Fig. 4. The measurement noise obtained as intercept values of the Kamaya's plots is found to be increasing with ε_{eq} for both step sizes as the uncertainty in orientation determination increases with deformation accumulating in the crystal owing to the lowering of pattern quality and increasing probability of pattern overlap [23,35]. The physical resolution limits of the EBSD detector also contribute to the uncertainties in orientation determination and hence the noise [36]. In order to gauge such a noise contribution in the orientation measurement in EBSD maps, misorientation distributions were calculated for ten different crystal orientations in recrystallized aluminum. The misorientation distributions for neighboring point pairs with the 1st neighbor were determined for a 5×5 μm^2 area and are plotted in Fig. 5 (a), where it can be observed that the different distributions are centered at ~0.4°. The average misorientation angle between neighboring point pairs (Kernel Average Misorientation - KAM) and all point pairs (Grain Orientation Spread - GOS) for all the ten different grain orientations are shown in Fig. 5 (b) and average values of 0.43 and 0.31° can be discerned, respectively. A close correlation between the average KAM and GOS values indicate that the orientations too away from the true orientation of the crystal are randomly distributed in the recrystallized material. The
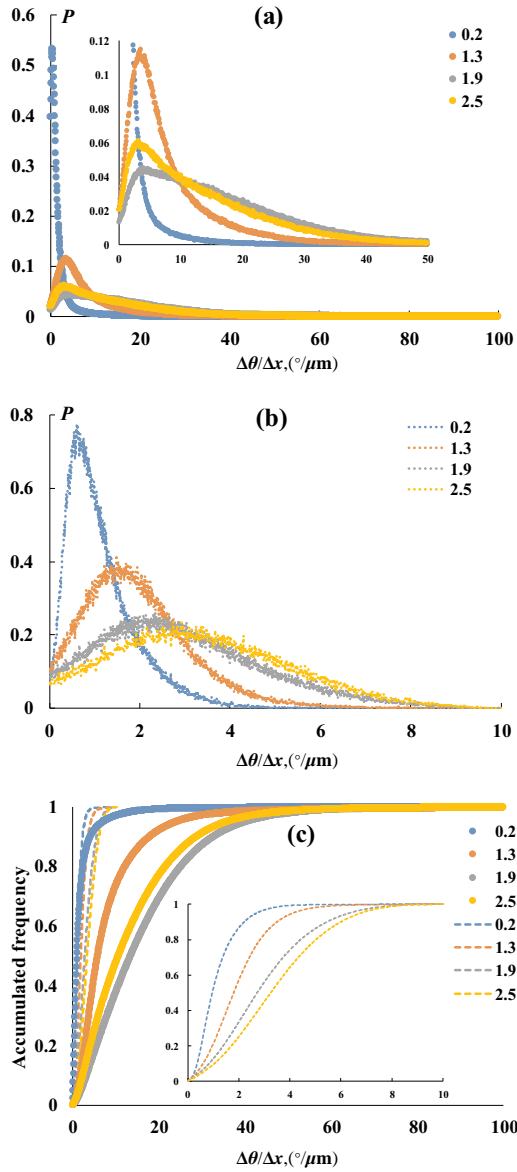
Fig. 3. Experimental probability density ((a) and (b)) and accumulated frequency (c) distributions for EBSD mapping data obtained with 0.1 μm (a) and 1 μm (b) step size for DHPT samples. In (c) broken line is for 1 μm (also shown in inset) and filled markers are for 0.1 μm data.

Table 1
Structural parameters observed experimentally and calculated using a double Rayleigh distribution for 1 and 0.1 μm step size EBSD mapping data at ε_{eq} of 0.2, 1.3, 1.9 and 2.5.

Structural parameters	EBSD scan step size							
	1 μm				0.1 μm			
	SPD strain							
	0.2	1.3	1.9	2.5	0.2	1.3	1.9	2.5
Experimental								
$\overline{\Delta\theta/\Delta x}$ (°/μm)	1.2	2.0	3.0	3.4	2.0	8.4	16.2	13.6
Double Rayleigh distribution								
$\overline{\Delta\theta/\Delta x}_{GNB}$ (°/μm)	1.7	2.3	3.2	3.5	4.3	14.8	20.7	18.6
$\overline{\Delta\theta/\Delta x}_{IDB}$ (°/μm)	0.8	1.4	1.1	0.4	0.9	4.6	6.5	5.2
ξ_{GNB}	0.41	0.61	0.87	0.96	0.25	0.34	0.66	0.6
Measurement noise, (°)	1.2	3.3	4.6	4.7	0.5	1.0	1.8	1.7
Null frequency pixels, (%)[a]	4.6	6.6	14.1	17.4	12.2	6.8	6.5	8.0

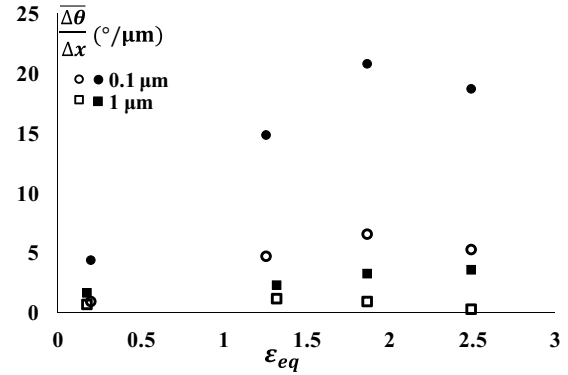[a] Pixels with $\frac{\Delta\theta}{\Delta x} = 0$.

Fig. 4. Mean misorientation gradient vs. ε_{eq} modeled for IDBs and GNBs for two different step size EBSD mapping data. (solid markers – GNBs; open markers – IDBs).

measurement noise at the lowest strain for 0.1 μm step size is quite close to that observed in the annealed material, which is clearly not the case for the 1 μm step size, where generally higher values are obtained for the orientation noise.

At low deformation levels, there is a possibility of crystal orientations fluctuating within the range of measurement noise, which results in a negative misorientation gradient [17]. The population of such pixels should drop with an increase in deformation in the material since increasing dislocation densities necessarily develop higher misorientations and thereby positive gradients. Such pixels are assigned a zero value and are given as null pixel frequency, N_p (%) in Table 1. The pixels with confidence index less than 0.1 in the processed EBSD maps are also included in the N_p values. From Table 1 it can be seen that N_p decreases with increasing ε_{eq} for 0.1 μm step size, except at the highest strain. Contrarily, for 1 μm step size, the N_p increases with ε_{eq}. Chen et al. observed that for a certain grain size, the fraction of the non-indexed points is directly proportional to the step size of the EBSD data acquisition in coarse as well as ultrafine-grained Titanium [37]. Similarly for the EBSD

maps recorded with 1 μm step size, with increasing ε_{eq} there can be a higher propensity of pattern overlap [23], which can act as a considerable factor contributing to a larger population of pixels with low confidence index and hence higher N_p. In the case of 0.1 μm EBSD step size at a ε_{eq} of 2.5, the effect of decreasing cell size and thereby increased fraction of non-indexed pixels clearly outweighs the effect of increasing misorientation gradients calculated at individual pixels.

A substantial difference is observed between the mean misorientation gradients modeled for both IDBs and GNBs at two step sizes, cf. Fig. 4, which either means that there exists a very large amount of SSDs within the deformed material or the developed substructure is considerably finer and thereby remains unresolved in the 1 μm step size EBSD maps. In Fig. 6, using point-to-point misorientation profiles in 0.1 μm EBSD maps, the average boundary spacing calculated for different minimum misorientation angles viz. 2, 5, 10, and 15° is plotted for ε_{eq} up to 4.5. It can be seen that above $\varepsilon_{eq} = 1.3$ and 2.5, the boundary structures having minimum misorientation angle of 2 and 5°, respectively decrease to a size below 1 μm and thereby the ensuing misorientation gradients would remain largely undetected in 1 μm EBSD maps. Fig. 7 shows the grain boundary maps for ε_{eq} 0.2–4.5, with boundaries indicated using black color for 10–15°, green color for 5–10° and red color for 2–5° misorientation. From grain boundary maps, it is evident that low misorientation boundaries having minimum misorientation of 2 and 5° form a significant portion of the total grain boundary area in the DHPT deformed samples at higher strains. If these boundaries are undetected and thus neglected from the substructure analysis, appreciable errors can be
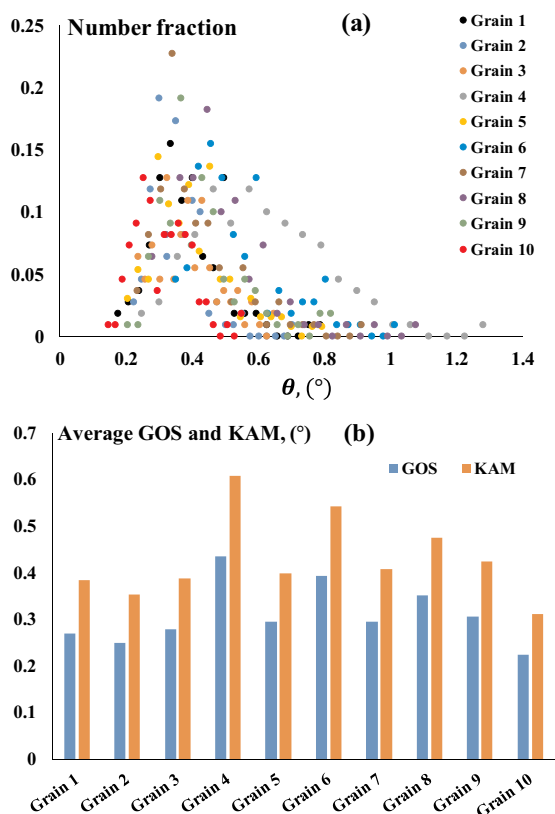
Fig. 5. Misorientation distributions calculated for ten different crystal orientations for the recrystallized material: (a) KAM distribution (θ_{ij}) for 1st neighbor and (b) average KAM and GOS.
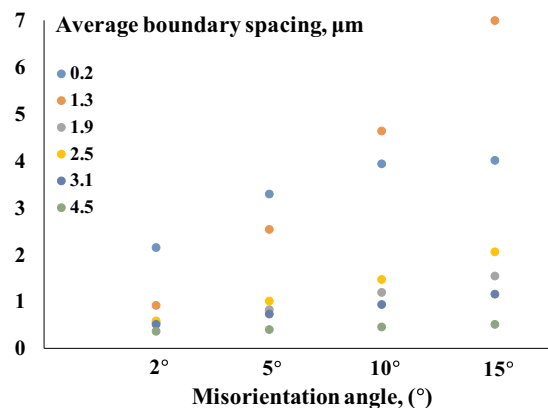

Fig. 6. Average boundary spacing calculated for different minimum misorientation angles, viz. 2, 5, 10, and 15° with increasing ε_{eq} for DHPT samples.

introduced in the subsequent statistical fitting of the experimental misorientation gradients. Hence a step size of 0.1 μm is considered suitable to investigate the deformation structures formed as a result of SPD in two different modes, i.e. static and dynamic and perform the statistical analysis of the rotation boundaries.

Additionally, during the present investigation, the results of the statistical modeling of misorientation gradients are observed to be sensitive to the kernel diameter size. Hence in order to choose a kernel diameter of the order of the same magnitude as that of the dislocation cell observed at the highest strain investigated, the local misorientation (θ_{ij}) for an ith neighbor with $i = 1$ to 3 are considered for further investigation of the static and dynamic HPT material, giving an effective kernel diameter of 0.4 μm.

3.2. Substructure evolution during HPT and DHPT

The experimental and modeled misorientation gradients along with other relevant structural parameters after fitting the double Rayleigh distribution for HPT and DHPT samples are given in Table 2. From experimental misorientation gradients, it can be seen that the high strain rate during DHPT introduces substructure in the material at a slightly faster rate than that in HPT, i.e. the same level of deformed structure is produced at a lower strain in DHPT material. In Table 2 (1st and 2nd row), the modeled mean misorientation gradients obtained for combined IDBs and GNBs are quite close to the mean misorientation gradients observed for the experimental distribution data, which proves that statistical fitting of EBSD misorientation data is capable of dissociating different structural parameters of the grain fragmentation process in SPD materials. As shown in Fig. 8 (a), in DHPT material higher misorientation gradients are predicted for GNBs at all strains, while in case of IDBs such a tendency exists at low deformation strains when compared with their HPT counterparts. Using Eq. (5), the GNDD is calculated and plotted in Fig. 8 (b). However, the local misorientation value is substituted by misorientation gradients in Eq. (5) which makes the detected lattice curvature and thereby the calculated dislocation density independent of the length scale of the microstructure or the kernel size considered within a reasonable range [31]. As described earlier, the estimation of Nye's dislocation density tensor involves calculation of lattice curvature based on the local misorientation gradients for neighboring pixels [21]. Hence misorientation gradients determined using Kamaya's plot were used in Eq. (5) [17,35]. In a recent study, it was shown that with a value of 3 for χ, the dislocation densities calculated using Eq. (5) coincides with those determined using Nye's tensor [38]. Additionally, this approach allows eliminating the effect of measurement noise on the calculation of ρ_{GND}, since measurement noise is determined for each pixel in an EBSD map in contrast to a general value between 0.5 and 1.5° chosen for measurement noise, which leads to artificial dislocation densities [39].

As foreseen, the SPD at higher strain rates can be seen to produce a larger amount of substructure in the material in terms of the dislocation densities. These dislocations organize themselves in low energy dislocation configurations preserving their individual strain fields and leads to a net lattice curvature to generate independently deforming dislocation cell blocks within a coarse grain. In the present study, ξ_{GNB} predicted for SPD material in both static and dynamic conditions are slightly higher than those previously reported for conventionally cold rolled aluminum [13]. When compared between HPT and DHPT materials, a higher median value of 0.5 is observed for ξ_{GNB} in DHPT material, while it is 0.43 in HPT material.

Interestingly, the sum of squared differences of fitting for the double Rayleigh distribution to the experimental data is found to be showing a positive trend with the increasing deformation strain (Table 2). Previously, it was observed that at higher deformation levels, when individual misorientation data of IDBs and GNBs are fitted with double Rayleigh distribution, two sets of boundaries, i.e. IDB₁, IDB₂ and GNB₁, GNB₂, respectively could be identified for each distribution [13]. The double Rayleigh fitting, thus generated two different mean misorientation angles for each distribution, which increased with the accumulation of deformation in the material. The evolution of the misorientation angle across the dislocation boundaries thus seems to be sensitive to other structural parameters. The crystal orientation, in which boundaries are formed, was found to have a considerable effect on the angular evolution of the IDBs and GNBs, as well as the morphology of such dislocation boundaries [40]. Therefore fitting of the double Rayleigh distribution to the EBSD data which combines the IDBs and GNBs seems to be an oversimplification for a comparatively complex process where multiple structural parameters may have an influence on the evolution of dislocation structure and associated boundaries.

The Vickers microhardness measurements were performed at different radii for disk and ring samples for HPT and DHPT materials,
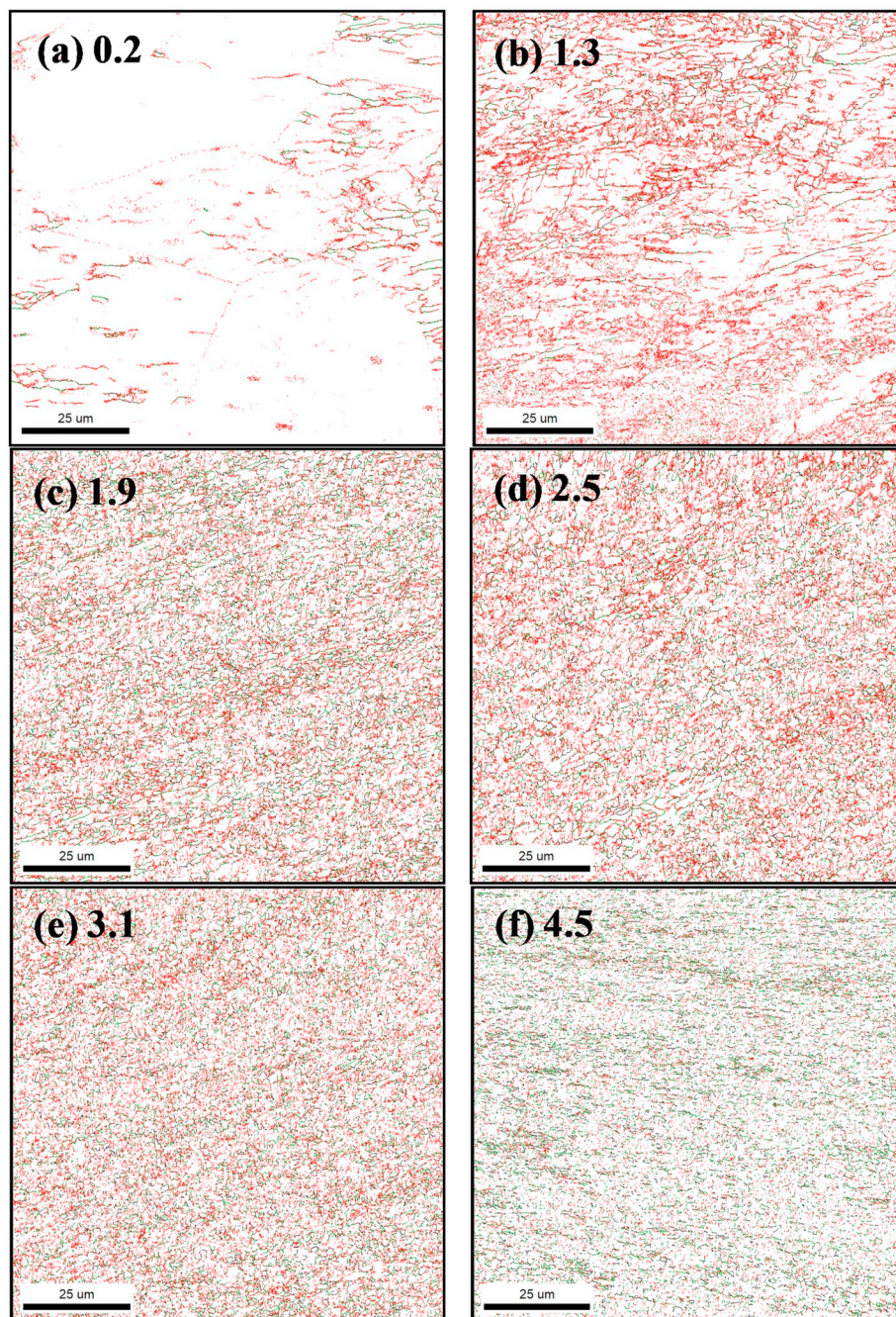
Fig. 7. Grain boundary maps for DHPT samples deformed to ε_{eq} of 0.2, 1.3, 1.9, 2.5, 3.1 and 4.5, with boundaries indicated using black color for 10–15°, green color for 5–10° and red color for 2–5° misorientation. (For interpretation of the references to color in this figure, the reader is referred to the web version of this article.)

respectively. As shown in Fig. 9, the hardness evolution with ε_{eq} can be described using a simple equation: $HV = k\varepsilon_{eq}^{\;n}$ [41,42]. A log-log plot of the Vickers hardness and ε_{eq} provides the values of hardness coefficient and exponent and are shown in a table in Fig. 9 for both materials. A higher coefficient for DHPT material is in agreement with the micro-structural observation, where a slightly rapid build-up of misorientation gradients is manifested across both, the IDBs and GNBs. However, quite a closeness of the hardness values to saturation hardness in DHPT material produces a lower hardness exponent.

Read and Shockley, based on their dislocation model for LAGBs, calculated the energy per unit area of the grain boundaries [43]. Here, the energy of a boundary is determined as a function of the angular misfit and the orientation of the boundary. The quantitative expression is given as:

$$E = \left[\frac{Ga}{4\pi\,(1 - \nu)} \right] \theta\,[A - ln\theta] \tag{12}$$

where G is the modulus of rigidity, a is the lattice parameter, ν is the Poisson's ratio, and θ is the angle of misfit or misorientation angle. The quantity A is determined by the orientation of the boundary and the energy of the atoms at the location of dislocation and has a value of 0.23 [43]. In the present case, the total boundary energy content for both the HPT and DHPT materials is calculated by considering all the dislocation boundaries, i.e. IDBs and GNBs. Fig. 10 shows the evolution of boundary energy content with the SPD equivalent strain. As en-visaged, incommensurate with the misorientation gradients developed across the dislocation boundaries, in DHPT materials higher boundary energy content is obtained compared with the HPT material. The

Table 2

Comparison of various structural parameters observed experimentally and modeled using double Rayleigh distribution for static and dynamically deformed HPT samples.

Structural parameters	HPT							DHPT					
	0.2	0.53	1.16	2.02	2.52	4.19	5.58	0.2	1.26	1.87	2.5	3.12	4.5
Experimental													
$\overline{\Delta\theta/\Delta x}$ (°/μm)	2.0	3.3	5.7	10.1	13.0	15.1	16.0	2.3	9.1	15.3	13.2	17.2	19.8
Double Rayleigh fitting													
$\overline{\Delta\theta/\Delta x}$ (°/μm)	1.8	3.1	5.4	9.8	12.6	14.7	15.3	2.0	8.1	14.8	12.6	16.4	19.1
$\overline{\Delta\theta/\Delta x}_{GNB}$ (°/μm)	3.2	5.9	12.7	17.5	20.7	23.0	26.3	5.1	19.0	23.8	21.9	26.3	31.0
$\overline{\Delta\theta/\Delta x}_{IDB}$ (°/μm)	0.9	1.6	2.4	4.0	5.1	5.4	4.6	1.0	3.7	4.9	4.2	5.3	4.3
ξ_{GNB}	0.39	0.37	0.3	0.43	0.48	0.53	0.49	0.27	0.29	0.52	0.47	0.53	0.55
Measurement noise, (°)	0.4	0.4	0.6	1.0	1.3	1.5	1.5	0.6	1.2	1.6	1.5	1.7	1.5
Null pixel frequency, (%)	14.9	9.4	8.0	5.9	5.7	7.8	13.6	25.8	17.1	10.3	13.5	13.8	10.3
SSD of fitting[a]	0.1	0.2	0.4	0.3	0.3	0.3	0.6	0.2	0.7	0.4	0.5	0.6	0.7

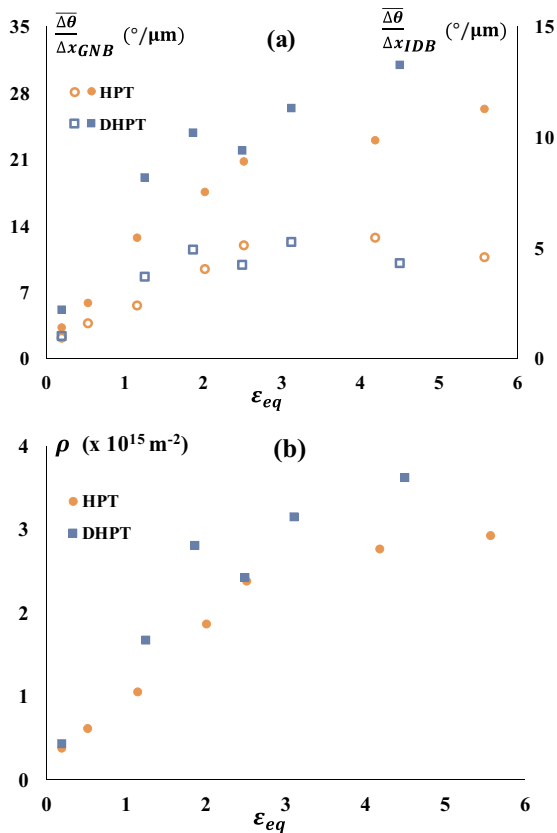[a] SSD – sum of squared differences.

Fig. 8. (a) Mean misorientation gradients modeled for IDBs (open markers) and GNBs (solid markers) after fitting double Rayleigh distribution and (b) GNDD calculated using Eq. (5) for HPT and DHPT material vs. ε_{eq}.

Fig. 9. Log-log plot of the Vickers microhardness and equivalent SPD strain for HPT and DHPT material.
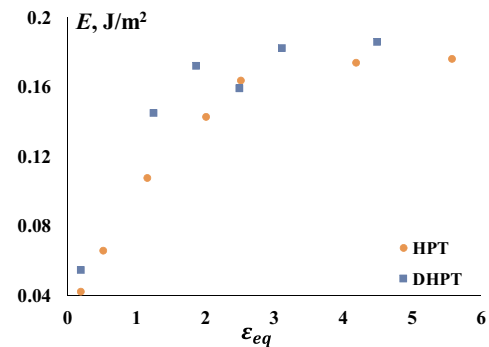
Fig. 10. The boundary energy per unit area calculated for both HPT and DHPT materials at various ε_{eq}.

boundary energy increases quite sharply initially, before showing a tendency for saturation above ε_{eq} of about 3.

3.3. Structural anisotropy – shear and radial plane

In order to investigate the anisotropy in structural evolution in the shear (RD-ϕ) and radial (ϕ-Z) planes, a HPT sample rotated to 180° was characterized on the respective planes of observation at three radial locations amounting to ε_{eq} of 4.19, 5.58, and 8.37. Fig. 11 shows the combined KAM and grain boundary maps for both the planes with boundaries having misorientation of 2–5°, 5–15° and 15–65° colored red, blue and black, respectively. Unlike in the shear plane, the radial plane shows a morphological texture in the shear direction. Though the
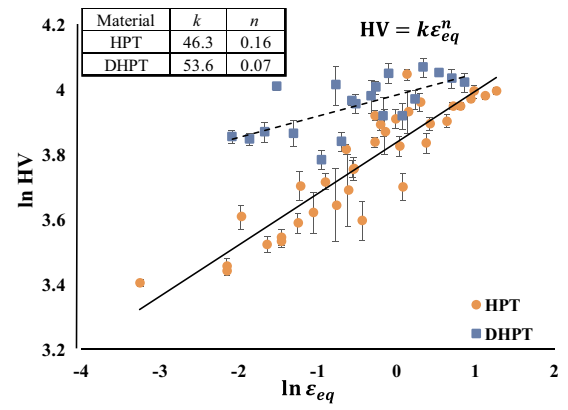
difference is not clearly visible for the LAGBs, a higher proportion of high angle grain boundaries (HAGBs) can be easily detected in the radial plane, especially at ε_{eq} of 8.37. The average KAM values for the maps from Fig. 11 are plotted vs. ε_{eq} in Fig. 12 (a). The local misorientation in the radial plane is higher during the fragmentation stage generally observed for the commercial purity aluminum [29] but comes closer to values identified in the shear plane at ε_{eq} = 8.37. The boundary length fractions for 2–5°, 5–15° and 15–65° boundaries present in both planes at different ε_{eq} are calculated and shown in Fig. 12 (b). At ε_{eq} = 4.19, 2–5° boundaries are more in the radial than in the shear plane, but the proportion of 5–15° and 15–65° boundaries, though close is lower in the radial plane. With increasing ε_{eq}, the fraction of the 2–5° and 5–15° boundaries continues to decrease in the radial plane compared to the shear plane. On the contrary, the 15–65° boundary
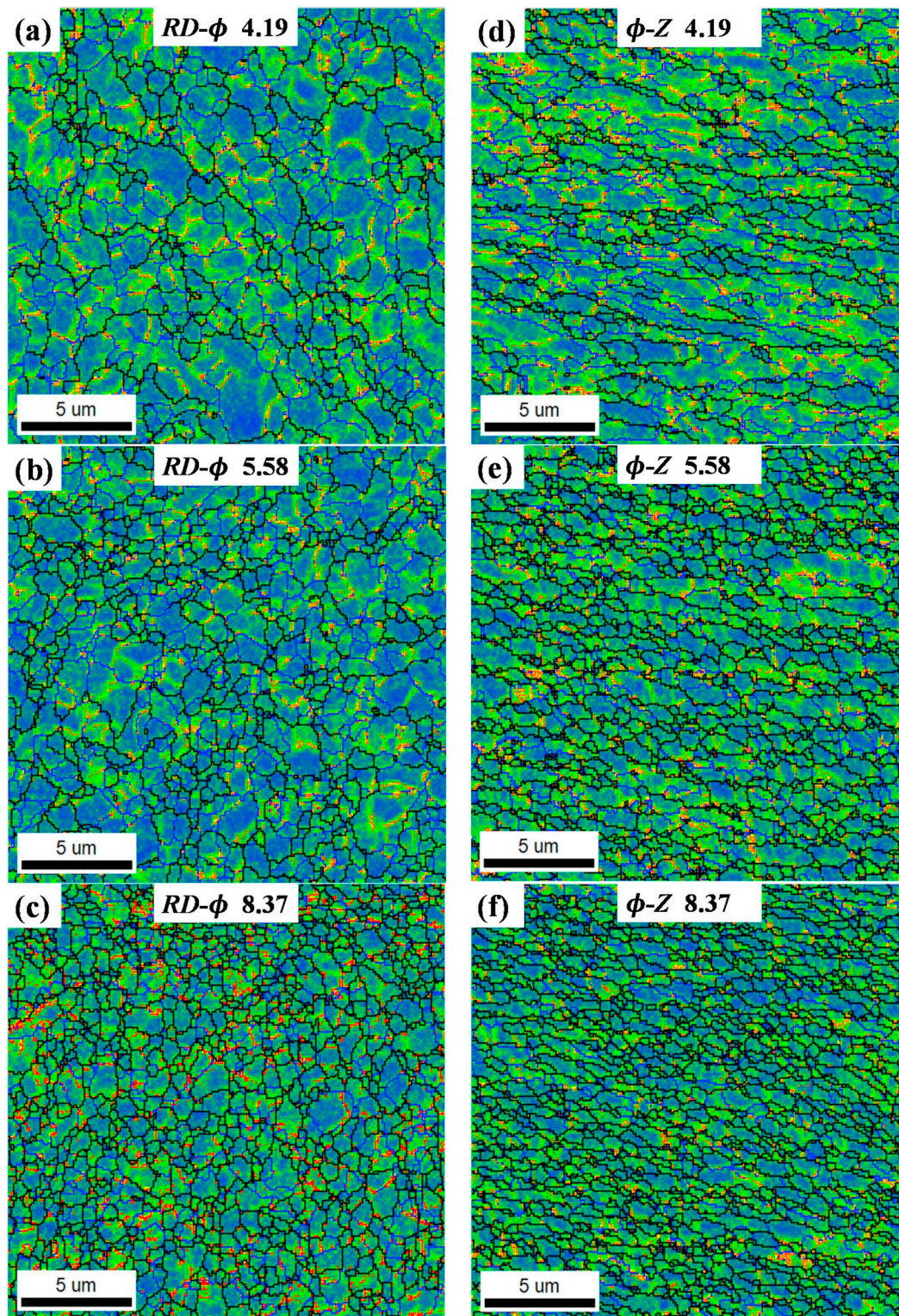
Fig. 11. Combined KAM and grain boundary maps for shear (a)-(c) and radial (d)-(f) planes, with boundaries having misorientations of 2–5°, 5–15°, and 15–65° colored red, blue and black, respectively, at different ε_{eq} of 4.19 (a) and (d), 5.58 (b) and (e) and 8.37 (c) and (f). (For interpretation of the references to color in this figure, the reader is referred to the web version of this article.)

length fraction continues to increase in the radial plane. Thus it can be seen that the newly forming HAGBs, nearing the saturation stage at larger deformation strains, can be more readily observed in the radial plane than in the shear plane, which implies that these new HAGBs are more parallel to the shear plane than with the radial plane.

Table 3 gives the experimental misorientation gradients and various

calculated structural parameters for both planes. Fig. 13 (a) shows the experimental misorientation gradients observed for both planes at three different deformation strains and distinct differences between them are clearly visible. In the case of the *RD-ϕ* plane, the experimental mean misorientation gradient increases with ε_{eq}, which is the result of increasing misorientation gradient across both GNBs and IDBs (see Fig. 13
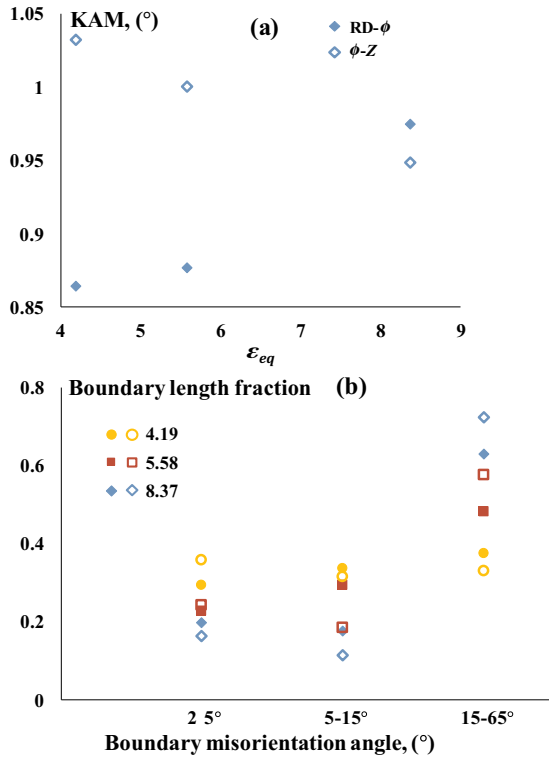
Fig. 12. Average KAM plotted vs. ε_{eq} for shear and radial planes in (a), while (b) shows the boundary length fractions calculated for boundaries having misorientation angle of 2–5°, 5–15°, and 15–65°, for both the planes at ε_{eq} of 4.19, 5.58 and 8.37 (Markers: solid-shear plane, open- radial plane).

(b)). The GNB fraction on the shear plane increases to 0.56 at ε_{eq} of 5.58 before descending to a value of 0.51 at ε_{eq} = 8.37, which is similar to the level observed at ε_{eq} = 4.19. From Fig. 13(c), in the ϕ-Z plane, on the other hand, the experimental mean misorientation gradient, though larger at ε_{eq} = 4.19, is relatively constant thereafter, in spite of continuously increasing misorientation gradient across GNBs. Such a behavior can be ascribed to the steadily dropping misorientation gradient across the IDBs and their corresponding frequency in the overall substructure on the radial plane.

For commercially pure aluminum, during HPT deformation a transition between the fragmentation and steady-state stage was observed at a strain of ~10 [19,31]. However, the structural parameters, e.g. misorientation gradients across GNBs and IDBs, and GNB fraction in the material starts progressing towards the saturation much before arriving at such transition deformation levels [31]. The mean misorientation gradient for GNBs and IDBs, was observed to be subsiding at

Table 3
Structural evolution across shear (*RD-ϕ*) and radial (*ϕ-Z*) planes in HPT deformed samples.

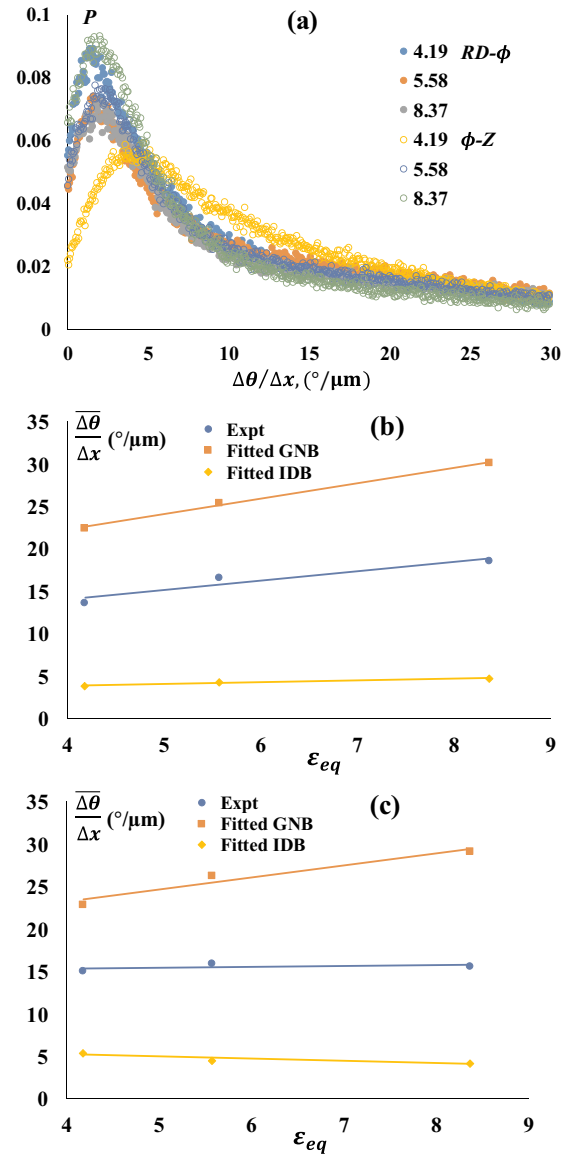| Structural parameters	Shear plane			Radial plane		
	4.19	5.58	8.37	4.19	5.58	8.37
Experimental						
$\overline{\Delta\theta/\Delta x}$ (°/µm)	13.7	16.7	18.7	15.1	16.0	15.7
Double Rayleigh fitting						
$\overline{\Delta\theta/\Delta x}$ (°/µm)	13.3	16.1	17.8	14.7	15.3	14.7
$\overline{\Delta\theta/\Delta x}_{GNB}$ (°/µm)	22.5	25.4	30.1	23.0	26.3	29.2
$\overline{\Delta\theta/\Delta x}_{IDB}$ (°/µm)	3.9	4.4	4.8	5.4	4.6	4.2
ξ_{GNB}	0.51	0.56	0.51	0.53	0.49	0.42
Measurement noise, (°)	1.3	1.5	1.5	1.5	1.5	1.4
Null pixel frequency, (%)	8.9	9.6	14.3	7.8	13.6	18.3
SSD of fitting	0.4	0.5	0.8	0.3	0.6	0.8

Fig. 13. (a) Experimental misorientation gradients calculated for shear and radial planes of a 180° rotated HPT sample at three radial locations amounting to ε_{eq} of 4.19, 5.58, and 8.37, and mean misorientation gradient values plotted vs. ε_{eq} for experimental data, fitted GNB and fitted IDBs for (b) shear plane and (c) radial plane. Solid lines in (b) and (c) – guide to the eye.

intermediate strain levels between 5 and 9, and the GNB fraction showed a peak at ε_{eq} of 5.6 before diminishing to the lowest value at ε_{eq} of 27.9. Thus from above observations, it can be conjectured that the substructures exhibited on the shear and radial planes in HPT deformed sample are at different stages of their transition towards the steady-state and though the differences are modest, they are clear enough to indicate the existence of anisotropy in microstructural evolution across these two planes. Such discrepancies in microstructural progression along different directions in the bulk material are bound to contribute towards the anisotropic response observed during subsequent mechanical testing.

4. Conclusions

Based on the observations made and their discussion following conclusions can be drawn:

1. At larger EBSD step size of 1 µm, a significant portion of the dislocations and thereby the orientation gradients generated by them

were unresolved. This is because, at moderate to large strains, a large proportion of dislocation structure having a minimum misorientation angle of 2 and 5° reached length scales much smaller than 1 μm.

2. Overall the accumulating strain distorted the crystal more and thus increased the measurement noise. However, the lower spatial resolution in 1 μm step size maps caused higher measurement noise and an increase in null value pixel frequency with increasing strain, possibly owing to a higher propensity for pattern overlap in a more refined structure.

3. In DHPT material, in contrast to HPT samples, a higher mean misorientation gradient for dislocation boundaries and larger median for GNB frequency was observed, resultantly contributing towards higher stored energies and hardness coefficient.

4. Anisotropic substructure evolution was observed on the shear and radial planes of an HPT deformed sample when investigated at different stages of deformation.

5. In spite of best efforts, the statistical fitting of double Rayleigh distribution for combined IDB and GNB data deteriorates at higher deformation strain. This is because the evolution of these boundaries is influenced simultaneously by multiple structural parameters during plastic deformation and hence fitting of double Rayleigh distribution proves to be an oversimplification of an otherwise complex process.

Funding

Data availability

The raw/processed data required to reproduce these findings cannot be shared at this time as the data also forms part of an ongoing study.

Declaration of competing interest

The authors declare that they have no known competing financial interests or personal relationships that could have appeared to influence the work reported in this paper.

References

[1] V.M. Segal, Methods of Stress-Strain Analyses in Metal Forming, Ph. D. Thesis Physical Technical Institute Academy of Sciences of Buelorussia, Minsk, Russia, 1974.
[2] V.M. Segal, Materials processing by simple shear, Mat. Sci. Eng. A 197 (1995) 157–164.
[3] Y. Saito, H. Utsunomiya, N. Tsuji, T. Sakai, Novel ultra-high straining process for bulk materials - development of the accumulative roll-bonding (ARB) process, Acta Mater. 47 (2) (1999) 579–583.
[4] P.W. Bridgman, On torsion combined with compression, J. Appl. Phys. 14 (1943) 273–283.
[5] N.A. Smirnova, V.I. Levit, V.I. Pilyugin, R.I. Kuznetsov, L.S. Davydova, V.A. Sazonova, Evolution of the fcc single-crystal structure during severe plastic-deformations, Fiz. Met. Metalloved. 61 (6) (1986) 1170–1177.
[6] A.P. Zhilyaev, T.G. Langdon, Using high-pressure torsion for metal processing: fundamentals and applications, Prog. Mater. Sci. (2008) 893–979.
[7] X. Sauvage, G. Wilde, S.V. Divinski, Z. Horita, R.Z. Valiev, Grain boundaries in ultrafine grained materials processed by severe plastic deformation and related phenomena, Mater. Sci. Eng. A 540 (2012) 1–12.
[8] G. T. Gray III, "High-strain-rate deformation: mechanical behavior and deformation substructures induced," Annu. Rev. Mater. Res., vol. 42, pp. 285–303, 2012.
[9] P. Verleysen, H. Lanjewar, Dynamic high pressure torsion: a novel technique for dynamic severe plastic deformation, J. Mater. Process. Technol. 276 (2020).
[10] D. Kuhlmann-Wilsdorf, Theory of plastic deformation:- properties of low energy dislocation structures, Mater. Sci. Eng. A 113 (1989) 1–41.
[11] N. Hansen, New discoveries in deformed metals, Metall. Mater. Trans. A 32 (2001) 2917–2935.
[12] B. Bay, N. Hansen, D.A. Hughes, D. Kuhlmann-Wilsdorf, Evolution of F.C.C. deformation structures in polyslip, Acta Metall. Mater. 40 (2) (1992) 205–219.
[13] W. Pantleon, N. Hansen, Dislocation boundaries - the distribution function of disorientation angles, Acta Mater. 49 (2001) 1479–1493.
[14] D.A. Hughes, Q. Liu, D.C. Chrzan, N. Hansen, Scaling of microstructural parameters: misorientations of deformation induced boundaries, Acta Mater. 45 (1) (1997) 105–112.
[15] D. Kuhlmann-Wilsdorf, LEDS: properties and effects of low energy dislocation structures, Mater. Sci. Eng. A 86 (1987) 53–66.
[16] C. Moussa, M. Bernacki, R. Besnard, N. Bozzolo, About quantitative EBSD analysis of deformation and recovery substructures in pure Tantalum, 36th Risø International Symposium on Materials Science, 2015 Roskilde, Denmark.
[17] C. Moussa, M. Bernacki, R. Besnard, N. Bozzolo, Statistical analysis of dislocations and dislocation boundaries from EBSD data, Ultramicroscopy 179 (2017) 63–72.
[18] W. Pantleon, On the statistical origin of disorientations in dislocation structures, Acta Mater. 46 (2) (1998) 451–456.
[19] S. Naghdy, P. Verleysen, R. Petrov, L. Kestens, Resolving the geometrically necessary dislocation content in severely deformed aluminum by transmission Kikuchi diffraction, Mater. Charact. 140 (2018) 225–232.
[20] J.F. Nye, Some geometrical relations in dislocated crystals, Acta Metall. 1 (1953) 153–162.
[21] W. Pantleon, Resolving the geometrically necessary dislocation content by conventional electron backscattering diffraction, Scr. Mater. 58 (2008) 994–997.
[22] L.P. Kubin, A. Mortensen, Geometrically necessary dislocations and strain-gradient plasticity: a few critical issues, Scr. Mater. 48 (2003) 119–125.
[23] A.J. Schwartz, M. Kumar, B.L. Adams, D.P. Field, Electron Backscatter Diffraction in Materials Science, Springer science and business media, LLC, New York, USA, 2009.
[24] J. Jiang, T.B. Britton, A.J. Wilkinson, Measurement of geometrically necessary dislocation density with high resolution electron backscatter diffraction: effects of detector binning and step size, Ultramicroscopy 125 (2013) 1–9.
[25] T.J. Ruggles, T.M. Rampton, A. Khosravani, D.T. Fullwood, The effect of length scale on the determination of geometrically necessary dislocations via EBSD continuum dislocation microscopy, Ultramicroscopy 164 (2016) 1–10.
[26] B.L. Adams, J. Kacher, EBSD-based microscopy: resolution of dislocation density, Comput. Mater. Contin. 14 (3) (2009) 185–196.
[27] D.A. Hughes, N. Hansen, D.J. Bammann, Geometrically necessary boundaries, incidental dislocation boundaries and geometrically necessary dislocations, Scr. Mater. 48 (2003) 147–153.
[28] T. Ruggles, PhD Thesis: Characterization of Geometrically Necessary Dislocation Content With EBSD-Based Continuum Dislocation Microscopy, Brigham Young University, Provo, Utah, USA, 2015.
[29] S. Naghdy, PhD Thesis, Texture and Microstructure Formation in Commercially Pure Aluminum During High Pressure Torsion, Ghent University, Ghent, 2017.
[30] B. Völker, N. Jäger, M. Calin, M. Zehetbauer, J. Eckert, A. Hohenwarter, Influence of testing orientation on mechanical properties of Ti45Nb deformed by high pressure torsion, Mater. Des. 114 (2017) 40–46.
[31] H. Lanjewar, S. Naghdy, F. Vercruysse, L.A.I. Kestens, P. Verleysen, Severe plastically deformed commercially pure aluminum: substructure, micro-texture and associated mechanical response during uniaxial tension, Mat. Sci. Eng. A 764 (2019).
[32] H. Lanjewar, L. Kestens, P. Verleysen, A novel method for severe plastic deformation at high strain rate, 12th International Conference on the Mechanical and Physical Behaviour of Materials Under Dynamic Loading, Arcachon, France, 2018.
[33] C. Zener, J.H. Hollomon, Effect of strain rate upon plastic flow of steel, J. App. Phys 15 (1944) 22–32.
[34] H.J. McQueen, J.E. Hockett, Microstructures of aluminium compressed at various rates and temperatures, Metall. Trans. 1 (1970) 2997–3004.
[35] M. Kamaya, Assessment of local deformation using EBSD: quantification of accuracy of measurement and definition of local gradient, Ultramicroscopy 111 (2011) 1189–1199.
[36] F.J. Humphreys, Review grain and subgrain characterisation by electron backscatter diffraction, J. Mater. Sci. 36 (2001) 3833–3854.
[37] Y. Chen, J. Hjelen, S.S. Gireesh, H.J. Roven, Optimization of EBSD parameters for ultra-fast characterization, J. Microsc. 245 (2012) 111–118.
[38] P.J. Konijnenberg, S. Zaefferer, D. Raabe, Assessment of geometrically necessary dislocation levels derived by 3D EBSD, Acta Mater. 99 (2015) 402–414.
[39] W. He, W. Ma, W. Pantleon, Microstructure of individual grains in cold-rolled aluminum from orientation inhomogeneities resolved by electron backscattering diffraction, Mater. Sci. Eng. A 494 (2008) 21–27.
[40] Q. Liu, D.J. Jensen, N. Hansen, Effect of grain orientation on deformation structure in cold-rolled polycrystalline aluminium, Acta Mater. 46 (16) (1998) 5819–5838.
[41] M. Kawasaki, Different models of hardness evolution in ultrafine-grained materials processed by high-pressure torsion, J. Mater. Sci. 49 (2014) 18–34.
[42] M. Kawasaki, R.B. Figueiredo, Y. Huang, T.G. Langdon, Interpretation of hardness evolution in metals processed by high-pressure torsion, J. Mater. Sci. 49 (2014) 6586–6596.
[43] W.T. Read, W. Shockley, Dislocation models of crystal grain boundaries, Phys. Rev. 78 (3) (1950) 275–289.